Catalytic CO_2/CO Reduction: Gas, Aqueous and Aprotic phase

Alexander Bagger,[*] Oliver Christensen, Vladislav Ivaništšev, and Jan Rossmeisl

Department of Chemistry, University of Copenhagen, Universitetsparken 5, Copenhagen, Denmark
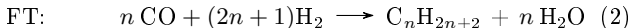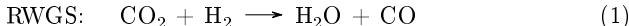
E-mail: alexander@chem.ku.dk

Abstract

The catalytic reduction of CO_2/CO is key to reducing carbon footprint and producing the chemical building blocks needed for society. In this work, we performed a theoretical investigation of the differences and similarities of the CO_2/CO catalytic reduction reactions in the gas, aqueous solution, and aprotic solution. We demonstrate that binding energy serves as a good descriptor for gaseous and aqueous phases and allows categorizing catalysts by reduction products. The CO vs. O and CO vs. H binding energies for these phases gives a convenient mapping of catalysts regarding their main product for the CO_2/CO reduction reactions. However, for the aprotic phase, descriptors alone are insufficient for the mapping. We show that a microkinetic model (including the CO and H binding energies) allows spanning and interpreting the reaction space for the aprotic phase.

Introduction

There is a call for turning the fossil based chemical industry into a sustainable one. A promising solution is the electrocatalytic production of carbon chemicals powered by electricity from renewable energy sources.[1]
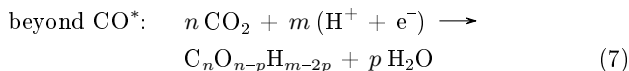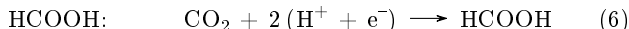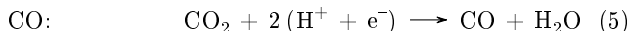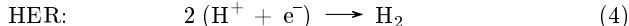
Today, the chemical industry produces primary chemicals such as methanol and high-value chemicals from an oil and gas feedstock. The conversion occurs in gas-phase catalytic reactions. Producing chemicals from syngas mixtures CO_2/CO+H_2 is the future. These are the Reverse Water Gas Shift (RWGS),[2] the Fischer–Tropsch (FT) process,[3,4] along with methanol (MeOH)[5,6] and higher alcohols[7] synthesis Let us write these reactions as:

$$RWGS: \quad CO_2 + H_2 \longrightarrow H_2O + CO \quad (1)$$
$$FT: \quad n\,CO + (2n+1)H_2 \longrightarrow C_nH_{2n+2} + n\,H_2O \quad (2)$$
$$MeOH: \quad CO + 2H_2 \longrightarrow CH_3OH \quad (3)$$

The product selectivity foremost depends on the metal catalyst and much less on the gas feedstock composition, ranging from CO+H_2 (syngas) to CO_2/CO+H_2 mixture. Active metals such as iron (Fe), cobalt (Co), ruthenium (Ru), and rhodium (Rh) are Fischer–Tropsch catalysts that can produce long carbon chains. Nickel (Ni) is less active and produces only methane (CH_4), while copper (Cu) in combination with oxophilic elements (e.g., Zn) can produce methanol.

The electrochemical CO_2/CO reduction reactions can enable the sustainable production of fuels and chemicals.[8] In the aqueous phase, the electrochemical CO_2/CO reduction reactions give carbon monoxide (CO), formic acid (HCOOH), high-value chemicals (e.g., CH_4, C_2H_4), and competitive hydrogen (H_2). Let us write these reactions as:

$$HER: \quad 2\,(H^+ + e^-) \longrightarrow H_2 \quad (4)$$
$$CO: \quad CO_2 + 2\,(H^+ + e^-) \longrightarrow CO + H_2O \quad (5)$$
$$HCOOH: \quad CO_2 + 2\,(H^+ + e^-) \longrightarrow HCOOH \quad (6)$$
$$beyond\ CO^*: \quad n\,CO_2 + m\,(H^+ + e^-) \longrightarrow$$
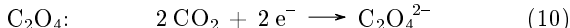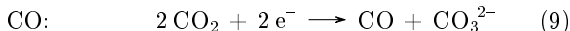$$C_nO_{n-p}H_{m-2p} + p\,H_2O \quad (7)$$

Here $*$ denotes the adsorbed species.

Similar to the gas-phase reductions, the selectivity in the aqueous phase depends on the metal catalyst. CO is produced on 11/12th group metals (Ag, Au, Zn) and HCOOH on p-block metals (Cd, In, Tl), high-value chemicals on Cu (labeled as "beyond CO^* products"). At the same time the competitive hydrogen evolution reaction (HER) takes place at the active metals (Fe, Ni, Pd, Pt). Note that we write formic acid as HCOOH although, above pH of 3.75, it is mainly in the form of $HCOO^-$.

Beyond the reduction reactions in the gaseous and aqueous phases, the aprotic non-aqueous electrochemical energy conversion of CO_2/CO should also be considered a promising method of reducing CO_2/CO *via* renewable energy. On the one hand, the absence of "easy" protons from H_2O in aprotic solutions prevents the competitive hydrogen evolution reaction (HER). Even a small admixture of water markedly enhance the HER kinetics, as demonstrated for Pt.[9] In the other hand, traces of H_2O or other proton sources is beneficial for CO_2/CO reduction to protonated species, as shown by the importance of H_2O for high-value carbon products on Cu(100).[10] Additionally, the aprotic electrolytes can contain specific compounds which have a blocking effect on the catalyst materials, such as the CN functional group in acetonitrile adsorbing on platinum electrodes.[11]

In the aprotic phase, electrochemical CO_2/CO reduction reactions produce mainly oxalate ($C_2O_4^{2-}$ which we denote in the text below as C_2O_4) and CO.[12] For CO production, which is carried out by protons and electrons in the aqueous phase, the reaction in the aprotic phase is assumed to occur through an oxygen species (O^{-*} which we denote in the text below as O^*) or carbonate (CO_3^{2-}):[13,14]

$$CO: \quad CO_2 + e^- \longrightarrow CO + O^{-*} \quad (8)$$
$$CO: \quad 2\,CO_2 + 2\,e^- \longrightarrow CO + CO_3^{2-} \quad (9)$$
$$C_2O_4: \quad 2\,CO_2 + 2\,e^- \longrightarrow C_2O_4^{2-} \quad (10)$$

These aprotic reactions are less studied than both the aqueous electrochemical and the gas-phase CO_2/CO reduction reactions.

Several examples show that aprotic reduction differs from aqueous one. In the aqueous phase, Cu produces a range

of products beyond CO^*. However, in acetonitrile (aprotic phase), Figueiredo *et al.* showed that the main reaction products from CO_2 reduction at Cu are carbonate, bicarbonate, and CO,[15] suggesting the carbonate reaction pathway. More active catalysts such as Fe/Ni sulfides show HER in aqueous and methanol electrolytes. However, the dominant HER is limited when changing the solvent/electrolyte.[16]

We should make a particular note for some electrolytes, such as methanol, where the behavior of protonation or access to protons can be similar to aqueous electrolytes. One example of this is shown by Ohta *et al.* for methanol-based supporting electrolytes on various metal electrodes at ambient temperature and pressure.[17] Besides controlling the electrolyte, the reference electrode can also be a challenge, as in the experiments by Ikeda *et al.*,[12] which was partly contaminated by Ag/Ag^+, as discussed by Tomita *et al.*[18]

In summary, we considered two important experimental conditions that could lead to a wrong conclusion when carrying out the analysis: i) water contamination and ii) electrode contamination. With this in mind, we investigated whether there is some relation between the product selectivity and the metal catalyst. We hypothesized that the CO_2/CO reduction reaction in the three phases (gaseous, aqueous, and aprotic) i) involve similar reaction intermediates, and ii) lead to different products depending on the catalyst and conditions. To investigate this hypothesis, we set out to explore *two scientific questions*:

- What are the catalytic differences and similarities between the gas, aqueous and aprotic phases for the CO_2/CO reduction reaction?

- How are the aprotic CO_2/CO reduction reactions products determined as a function of condition and catalyst?

To answer the *first question*, we focus on descriptors rather than reaction schemes, thus, abstracting away from the complete analysis of numerous pathways. In this way, we give a combined descriptor view of these reactions for direct comparison – to learn about the similarities and differences that dominate the reactions – without discussing the detailed mechanisms.

Previously, we have built a classification scheme for the electrochemical reduction of CO_2/CO in the aqueous phase (see Ref. 19) for comparing metal catalyst performance for the CO_2 reduction reaction. The scheme shows that CO_2 reduction on different metal surfaces can be divided into four groups based on the ΔE_{H^*} and ΔE_{CO^*} binding energies. This scheme shows the unique properties of the Cu catalyst compared to the other metals. Cu can bind CO without having H underpotential deposited, which we consider a prerequisite to allowing the reduction of gaseous CO.

In this work, we use the binding energy descriptors, which could have chemical importance for the reactions in the different phases: ΔE_{CO^*}, ΔE_{H^*}, ΔE_{O^*}, ΔE_{OH^*}, ΔE_{C^*}, ΔE_{COOH^*}, ΔE_{HCOOH^*}, along with the work function of the metals. One may think that these descriptor investigations needs to be under the assumptions that (a) the catalysts are affected by the environment in a similar way, (b) the trends in the low coverage regime capture essential features of the catalyst performance, and (c) the trends observed for given active facets correlate to those on other facets, including defects. However, when looking at the correlation between products and descriptors, you do not need assumptions, as long as the descriptor used is intrinsically related to the material and easy to obtain.

Note that these descriptor investigations are done under the assumptions that (a) the catalysts are affected by the environment in a similar way, (b) the trends in the low coverage regime capture essential features of the catalyst performance, and (c) the trends observed for given active facets correlate to those on other facets, including defects.

To answer the *second question* about the reduction in the aprotic phase, we built a microkinetic model accounting for the potential of protons (water) similarly to the experiments on Sn[20] and Pt,[18] where the H_2O content was varied. We validated the model on a series of aqueous,[21] aprotic,[12] and CO_2 pressure experiments.[22] Finally, we extrapolated the model across the ΔE_{CO^*} vs. ΔE_{H^*} description found for aqueous CO_2 electroreduction.

Results and discussion

Classification analysis

Figure 1 shows the classification scheme extended to include the gaseous and aprotic phases. Figures 1a–c present a cropped periodic table with the main products indicated by different colors. Below them, Figures 1d–f show the ΔE_{CO^*} vs. ΔE_{O^*}, ΔE_{CO^*} vs. ΔE_{H^*}, and ΔE_{CO^*} vs. ΔE_{H^*} descriptor plots used for the gas, aqueous and aprotic phases. These descriptors are chosen since they represent the clearest grouping of elements according to product (highlighted with color). In the descriptor plots, the data is displayed with the BEEF-vdW[23,24] error ellipse with respect to the Cu(111) facet. At the same time, the catalysts without a product in the above periodic table are left as a black point marker. The horizontal line depicts the CO binding vs. CO(g) and the vertical line depicts $\Delta G = 0$ for $H^* \rightleftharpoons \frac{1}{2} H_2$ (which distinguishes H_{UPD} catalysts, i.e., Under Potential Deposited hydrogen catalysts).

Figures 1a and 1d focus on the gas-phase, where the most insightful are the ΔE_{CO^*} vs. ΔE_{O^*} descriptors. Other descriptor plots have been tested and are shown in supplementary Figure S1. Note that the ΔE_{O^*} descriptor for the gas-phase reactions is known to be important and has previously been used to describe the NiGa and the CuZn catalyst system performance for methanol synthesis from CO_2.[5]

The metal catalyst data in Figures 1a and 1d illustrates that a Fischer–Tropsch catalyst (red) binds CO^* and O^* strongly, indicating that these catalysts can potentially bind and dissociate CO into C and O on the surface, which then gets reduced by H_2. Ni has moderate CO^* and O^* binding, which we believe allows Ni to reduce or dissociate CO. However, due to the moderate binding, Ni does not have a high carbon species coverage, producing only methane (yellow). Pd and Pt are given a blue, CO^* binding color, as these catalysts bind CO^* strong and O^* weak. That means that they get poisoned by CO^* due to the poor oxygen binding energy, which does not allow them to dissociate CO^* or getting the carbon off the active catalyst. For Cu, which catalyzes methanol (cyan) and higher alcohols formation in the gaseous phase,[7] the CO^* and O^* binding is weak but seems to be enough to bind CO^*. That is given by the fact that Cu is just below our horizontal line of binding CO^* vs. not binding CO^*. However, one should bear in mind that the chemical potential of CO in a gas-phase experiment can be varied significantly. These binding properties do not allow for the dissociation of CO^* but instead for protonation of CO^* toward the alcohol species, which can also desorb because of the weak carbon bond.
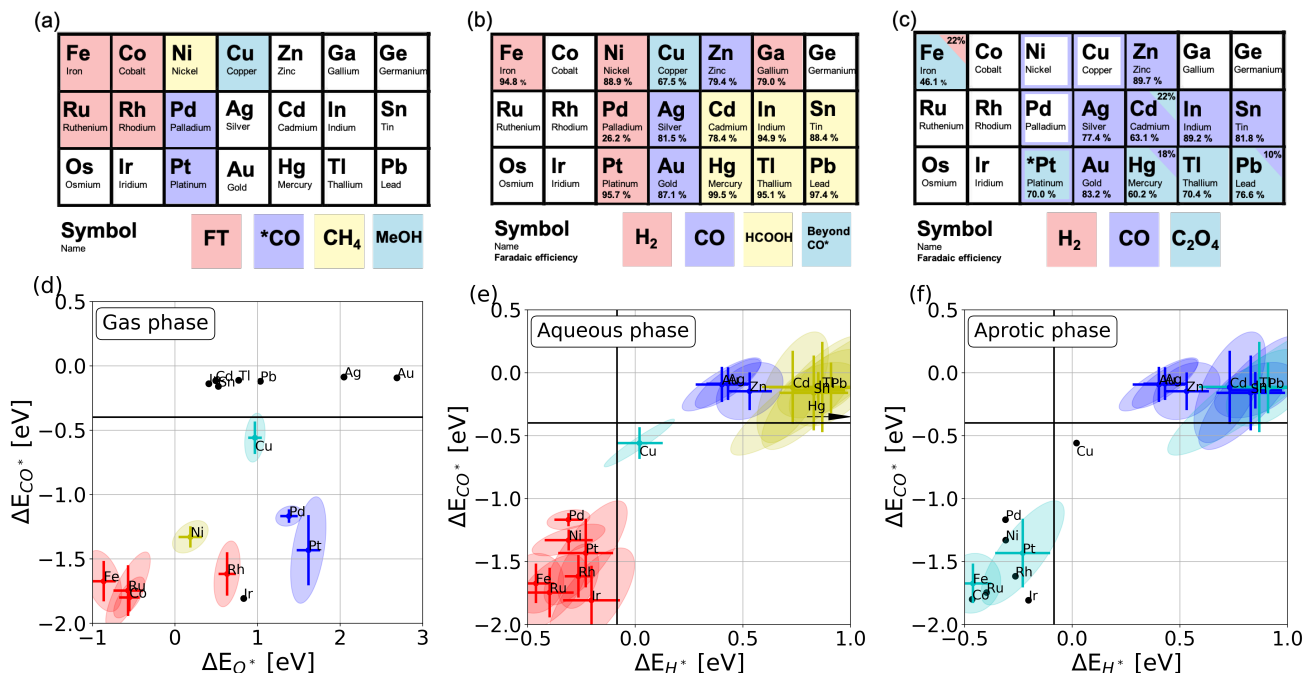
Figure 1: Cropped periodic tables with the main products and descriptor analysis of gaseous (a,d), aqueous (b,e), and aprotic (c,f) phase for CO_2/CO reduction reactions. Colors from the periodic table are used in the descriptor figure below. For the gaseous phase, the best visualization is CO^* vs. O^*, while for the aqueous and aprotic phase, it is CO^* vs. H^*. Other visualizations are given in supplementary. Note the oxalate and CO product mixing for the Cd, In, Sn and Hg, Tl, Pb catalysts for the aprotic phase. Note that Pt catalytic performance is chosen from Tomita et al.,[18] since Ikeda et al.[12] has been contaminated by the Ag/Ag$^+$ reference electrode. References used for products 2–6,12,18,19,21.

Figures 1b and 1e present the aqueous phase analysis of ΔE_{CO^*} vs. ΔE_{H^*} for the CO_2 reduction reaction.[19] There is a group of metals having H_{UPD}, which only produces H_2 (red). There are two groups which do not bind CO^*, giving either CO gas (blue) or formic acid HCOOH (yellow), depending on the H^* coverage during the reaction. Finally, Cu stands out as it binds CO and does not have H_{UPD}, giving a range of different products (green).

Figures 1c and 1f show a puzzling picture of the aprotic CO_2 reduction on the ΔE_{CO^*} vs. ΔE_{H^*} descriptors plot. Other descriptor plots are shown in supplementary Figures S2–S3; however, it was impossible to find a visualization that allows us to distinguish and give a clear representation of the CO and oxalate product formation from a descriptor analysis of the metal catalysts. Even correctly assigning the main product of the reduction by color in Figure 1c is challenging, as pointed out in the introduction. In this work, data by Ikeda et al.[12] is used, but for Ni, Pd, Pt, and Cu we only draw a blue frame around the elements as we believe these can have been contaminated by the Ag/Ag$^+$ reference electrode – this suspicion is based on the observation of a CO (blue) product formation, which is found on Ag. For Pt, noted by an asterisk, the experiment by Tomita et al.[18] is used and gives the oxalate (cyan) product.

In the aprotic phase, the Cd, In, and Sn elements produce mainly CO, while Hg, Tl, and Pb produce oxalate. That differs from the aqueous phase, where the p-block metals (Cd, In, Sn, Hg, Tl, and Pb) catalyze the formic acid formation. Carrying out analysis of several binding energies and work functions (see Figure S3) as descriptors for these elements in the periodic table, the descriptors for these metals are similar. Hence, the presented descriptor analysis does not distinguish between the different catalytic materials in the

aprotic phase. Furthermore, the product formation in the aprotic phase differs from the gaseous and aqueous phases. One example is that Pt and Hg – an active and inactive catalyst – both produce oxalate – albeit with different catalytic properties.

The difference observed between the gaseous, aqueous, and aprotic phases is that the driving force in the gaseous phase is given by the pressure difference and the temperature allowing the reaction to overcome the barrier for dissociation of CO. In contrast, in electrocatalysis, the reaction is driven by the potential. While the pressure can be varied, particularly in aprotic solutions, the temperature is typically low compared to gaseous phase, which limits the dissociation of molecules.

From the observed similarities, we can see that the carbon binding energy, in our case the CO^*, is a crucial parameter across the three different phases of CO_2 reduction at the metal catalyst investigated here.

Microkinetic model

The classification analysis reveals a complicated picture for the aprotic CO_2 reduction. Namely, as can be seen in Figure 1f, metals grouping does not distinguish between product formation. To clarify the picture, we formulated a simple microkinetic model to investigate how the product distribution varies with the concentration of H_2O and CO_2, see supplementary information for details. Microkinetic models can be formulated in various ways, and we consider our model as extremely simple with multiple assumptions to have a few parameter where we know exactly what they mean for the model and do not allow us to "over-fit" our experiments.

In the model, we assume that a charged CO_2^* reacts with

CO_2 forming the carbonate intermediate and CO as proposed in literature[14] (CO reaction 9), whereas coupling two charged CO_2^* leads to C_2O_4. Utilizing these reaction pathways for our microkinetic model works well at describing the change in product distribution when varying the concentration of H_2O and CO_2 in the following rate expressions:

$$r_{H_2} = \theta \cdot k_{H_2} \cdot n_{H_2O}^2 \cdot \exp\left(-\frac{\Delta E_{H^*}}{k_B T}\right) \tag{11}$$

$$r_{CO} = \theta \cdot k_{CO} \cdot n_{CO_2}^2 \cdot \exp\left(-\frac{\Delta E_{CO_2^*}}{k_B T} + \frac{\Delta E_{CO^*}}{k_B T}\right) \tag{12}$$

$$r_{HCOOH} = \theta \cdot k_{HCOOH} \cdot n_{H_2O} \cdot n_{CO_2} \cdot \exp\left(-\frac{\Delta E_{CO_2^*}}{k_B T}\right) \tag{13}$$

$$r_{C_2O_4} = \theta^2 \cdot k_{C_2O_4} \cdot n_{CO_2}^2 \cdot \exp\left(-\frac{2\Delta E_{CO_2^*}}{k_B T}\right) \tag{14}$$

$$\frac{1}{\theta} = \begin{array}{l} 1 + n_{H_2O} \cdot \exp(-\Delta E_{H^*}/k_B T) \\ + n_{CO} \cdot \exp(-\Delta E_{CO^*}/k_B T) \\ + n_{CO_2} \cdot \exp(-\Delta E_{CO_2^*}/k_B T) \end{array} \tag{15}$$

where k_{H_2}, k_{CO}, k_{HCOOH}, and $k_{C_2O_4}$ are four prefactors to adjust the absolute rates (these can be considered fitting parameters) and has the unit of s^{-1}, n_{H_2O} and n_{CO_2} is the concentration, ΔE_{H^*}, $\Delta E_{CO_2^*}$ and ΔE_{CO^*} are the respective binding energies, θ is the number of free sites, and $k_B T$ is the product of the Boltzmann constant and temperature. The assumptions made in deriving Eqs. 11–14 are given in the supplementary.

Recently, Rohr *et al.* formulated a similar microkinetic model for Pt.[13] Their model includes a dissociation step of CO_2 into CO and O^* (CO reaction i 8). Experimentally, for gas-phase catalysis, the dissociation reaction of CO_2 to CO and O^* and the subsequent formation of a carbonate species was shown on a Cu/Pt(111) system.[25] However, at a low temperature and electrolyte environment, the dissociation pathway may be challenging. Furthermore, the CO_2 dissociation model is challenged by the CO and C_2O_4 dependence on concentration found by Gennaro *et al.*[22]

Figures 2a and 2c show the product formation from CO_2 reduction experiments[18,20] on Sn and Pt with varying concentration of water (n_{H_2O}). As the water content is decreased, the solubility of CO_2 goes up, and hence the CO_2 concentration is increased. Furthermore, as experiments are carried out at constant current, the absolute potential decreases with decreasing water content to obtain similar currents. Hence, the experiments in Figures 2a and 2c goes from -2 V to -3.2 V vs. Fc/Fc$^+$ when decreasing the water content. Specifically for the reactions involving CO_2, it is to be noted that the CO_2 reduction potential to CO_2^- has been estimated to be -1.9 V, based on $E^\circ(Tl^+/Tl_{(aq)}) = -1.94$ V.[26] To simplify our model, and since calculating CO_2^- is a challenge, we assume the activated CO_2^- to have a constant strong binding. Furthermore, we assume a constant low pressure of CO.

Figures 2b and 2d show the predicted product distribution from the microkinetic model when the four parameters have been adjusted to the experimental data from Figures 2a and 2c. As the model results follow the experimental results well, it illustrates that this model can explain the product distribution from the two different catalysts when only using the ΔE_{H^*} and ΔE_{CO^*} binding energies for Pt and Sn across orders of magnitude in water content.

Figure 3 shows four bar plots of the experimental data

in (a) aqueous phase and (c) aprotic phase to be compared with the model predictions in (b) aqueous phase and (d) aprotic phase. Figures 3a and 3c use the experimental total faradaic efficiency as measured, whereas the data in Figures 3b and 3d is normalized to 100%. This comparison further validates the model by testing the model for other metal catalysts with different binding energies to Pt and Sn.

In aqueous electrolyte (Figures 3a and 3b), the model predicts HER for Fe, Ni, and Pt, similarly to the experimental results. As the model does not include a rate term for beyond CO^* products, the prediction for Cu is naturally not beyond CO^* products. Instead, the model predicts formic acid, which agrees nicely with experimental results on Cu[27] showing major H_2 and formic acid formation when discarding beyond CO^* products. Most interestingly, Ag and Au have different binding energies to both Pt and Sn, and our model predicts major CO formation, which is similar to the experimental results. However, the microkinetic model relies on the CO and carbonate pathway (Eq. 9), which differs greatly from the proposed proton–electron pathway (Eq. 5) and which is typically modeled by a critical COOH* intermediate.[28] Hence it seems that the carbonate reaction could be important for the reaction. The carbonate species were identified on Cu at intermediate potential (-0.3–0.3 V vs. RHE) by *in situ* surface-enhanced infrared absorption spectroscopy (SEIRAS)[29] and simulated as an essential intermediate in cyclic voltammetry on Cu.[30] Furthermore, our model predicts that Ag and Au have formic acid as a minor product, while the experiments show them to have minor HER.

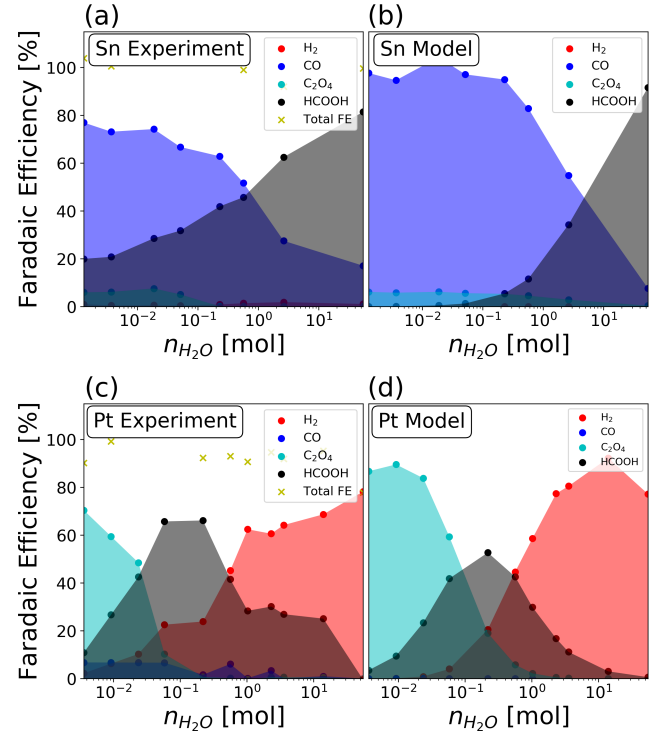Finally, for the metals experimentally producing formic

Figure 2: Comparison of the faradaic efficiency of products from CO_2 reduction reaction experiments by varying the H_2O content on (a) Sn and (c) Pt and the predicted product distribution from the microkinetic model for (b) Sn and (d) Pt. Experimental data from Refs. 18,20
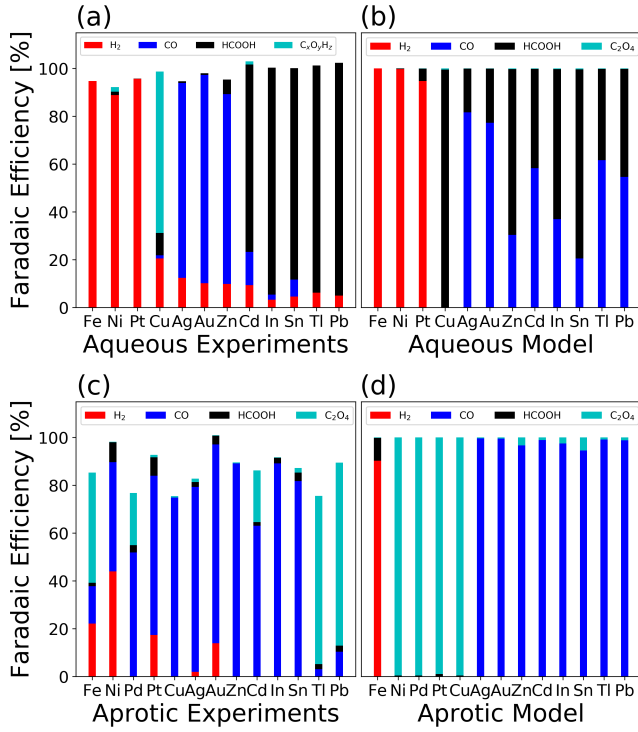
Figure 3: Comparison of the faradaic efficiency of products from CO_2 reduction reaction experiments in (a) aqueous and (c) aprotic phase and the predicted product distribution from the microkinetic model in (b) aqueous and (d) aprotic phase. For Cu, there is not included a specific reaction for beyond CO^* products in either phase. Note that (c) shows only the reported products for the metals from Ikeda et al.,[12] where Ni, Pd, Pt, and Cu catalytic performance is probably contaminated by Ag/Ag^+ reference electrode.

acid, our model predicts a mix of CO and formic acid, with weight on formic acid production.

In aprotic electrolyte, the experiments in Figure 3c display the results only from Ikeda et al.,[12] where parts of the metal catalytic performance is probably contaminated by the Ag/Ag^+ reference electrode, as mentioned above. Figure 3d shows the microkinetic model predicted product distribution for the aprotic solution, where the water content is set to $n_{H_2O} = 10^{-3}$. However, the level of H_2O present is unknown for the experimental results. For Fe, the model predicts primarily HER, which is also present at lower faradaic efficiency in the experiments. Besides this, the model predicts oxalate for the metals that bind CO^* (similar to Pt), and CO with oxalate as a minor product from the metals that do not bind CO. Interestingly enough, Au and Ag are again predicted correctly by the model. In contrast, the model does not describe the inactive p-metals producing oxalate compared to experimental faradaic efficiency. This discrepancy is important and is elucidated upon and discussed in the next section.

Figures 4a and 4b show the product distribution in aprotic electrolytes ($n_{H_2O} = 10^{-3}$) by varying the n_{CO_2} concentration for the Sn and Pt catalyst, respectively. Figure 4b shows the product distribution for Pt, which according to the model, produces mainly oxalic acid in the shown n_{CO_2} concentration range. For the Sn catalyst, as shown in Figure 4a, the microkinetic model predicts oxalate formation at low n_{CO_2} concentrations and CO at high concentrations.
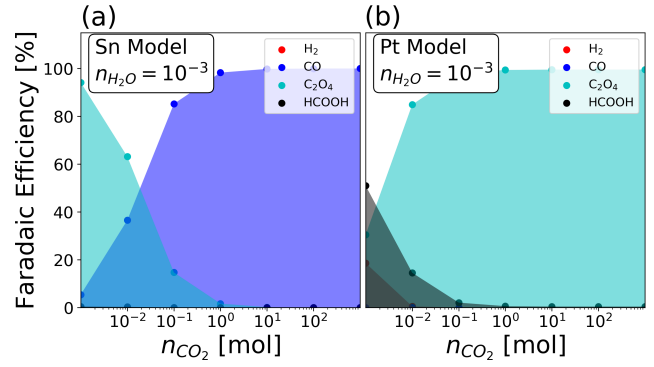

Figure 4: Predicted product distribution from the microkinetic model by varying the CO_2 concentration/pressure at (a) Sn and (b) Pt catalyst.

The latter result illustrates what could be seen in the experimental results for the p-metal catalysts by Ikeda et al.,[12] which switch between CO and oxalic acid production. It thus seems likely that the production of CO or oxalic acid is highly dependent on the accessibility or pressure of CO_2. That was also shown for experiments on Hg by Gennaro et al.,[22] where low concentrations of CO_2 produce oxalate and high concentrations of CO_2 produce CO. Note that these findings come directly out of the model due to the difference in r_{CO} and $r_{C_2O_4}$ which have θ and θ^2, respectively (see Eqs. 12 and 14). For the reaction mechanism, it means that oxalate requires two CO_2^* at the surface, while the production of CO only requires one CO_2^* at the surface in combination with one in solution.

Figure 5 presents the calculated product distribution in the ΔE_{CO^*} vs. ΔE_{H^*} picture, with the metals co-plotted (crosses) and the reference experimental results for Pt and Sn as square markers. This is valuable, as the CO^* binding is important for the reactions in combination with the H^* binding energy in order to explain the HER. In Figure 5, the concentrations of water (n_{H_2O}) and CO_2 (n_{CO_2}) are varied to show (a) aqueous phase, (b) aqueous phase with high CO_2 pressure, (c) aprotic phase and (d) aprotic phase with high CO_2 pressure. The ΔE_{CO^*} vs. ΔE_{H^*} illustrates how the product distribution behaves in four different "electrolyte settings" with respect to n_{H_2O} and n_{CO_2}.

Comparison of Figure 5a with Figure 5b reveals the effect of increasing the CO_2 pressure on the aqueous phase CO_2/CO reduction. The microkinetic model simulations here show that highly active metals Pd, Ni, Pt, etc., can reduce CO_2 at high pressures, which is in line with the high-pressure experiments in aqueous electrolytes.[31,32] The experiments show that the active metals produce formic acid (green area), which aligns with the model predictions. For beyond CO^* products for Cu, high-pressure CO_2 experiments on Cu show a limited HER and increased CO_2 reduction products.[33] However, this is not captured by the model, as a rate term for beyond CO^* products is not included. Note that at much higher pressures, above 73.8 bar, CO_2 reaches its supercritical conditions, and the model could break down. Experiments with supercritical CO_2 prevent significant hydrogen evolution and increases the production of hydrocarbons, organic acids, or alcohols.[34]

Moving from the aqueous to the aprotic environment, from Figure 5a to Figure 5c, show that the H_2 signal (red area) almost disappears and C_2O_4 (cyan area) production becomes dominant instead of formic acid (green area). Interestingly
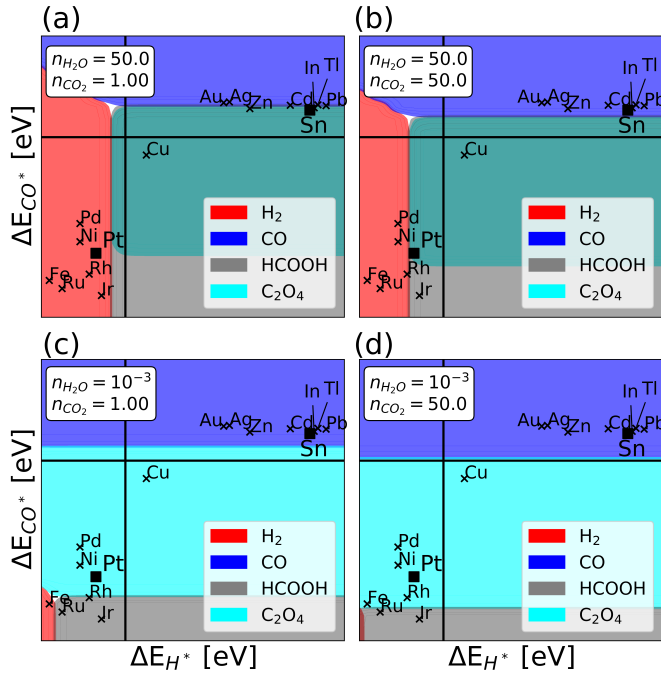
Figure 5: Predicted product distribution from the microkinetic model in the ΔE_{CO^*} vs. ΔE_{H^*} description for electrochemical CO_2 reduction. The n_{H_2O} and n_{CO_2} conditions for (a) can be considered aqueous phase, (b) aqueous phase with high CO_2 pressure, (c) aprotic phase with normal CO_2 pressure, and (d) aprotic phase with high CO_2 pressure. The metals are co-plotted (crosses) and the reference experimental results for Pt and Sn as square markers

enough, it shows that formic acid does indeed need protons, while the CO reaction does not. Further increasing the CO_2 pressure, from Figure 5c to Figure 5d, illustrates how H_2 product formation is further limited, but importantly also shows the competition between CO and C_2O_4 products. The figures show that increasing the CO_2 pressure increases the rate of CO production as compared to oxalate. We should make a final note on metallic Ir, which seems to produce HCOOH under all tested conditions.

Conclusions

In conclusion, we have carried out a classification analysis for gaseous, aqueous, and aprotic phases to determine the descriptors for the product distribution of the CO_2/CO reduction reactions. We have derived a microkinetic model and identified the most critical model parameters for analyzing the product distribution dependence on the H_2O and CO_2 concentration.

The classification analysis shows that the ΔE_{CO^*} and ΔE_{O^*} descriptors are significant for the gaseous phase. Differently, for aqueous and aprotic phases, ΔE_{CO^*} and ΔE_{H^*} are more appropriate. That is because the dissociation mechanism is dominant for the gaseous phase (at elevated temperatures), while in electrolytes the association mechanisms prevail (at ambient temperatures). The aprotic phase requires more careful analysis due to the lack of reliable experimental data and the need for accounting concentrations via microkinetic modeling.

Using a few assumptions and parameters, our microki-

netic model gives two exciting insights into the reaction: i) a carbonate pathway can model the CO product formation both in the aqueous and aprotic phase in agreement with the experiments; ii) the oxalate and CO product mixing in aprotic media is probably a result of changing the CO_2 concentration. The model shows that oxalate is formed from two adsorbed CO_2 and CO – from one adsorbed CO_2.

Although reaction for the high-value products from aqueous Cu (beyond CO^* products) is not included in our model. The experiments, our classification analysis, and the microkinetic model support that the high-value products observed from CO_2RR is a result of the combination of unique binding energies for the Cu catalyst and the aqueous environment, as previously found. [10]

Experimental

The simulations were run using ASE [35] with fixed bottom layers for four-layered metal slabs. A series of adsorption sites were tested, and the most stable sites were selected. The electronic calculations are carried out at the Generalized Gradient Approximation Density Functional Theory (GGA-DFT) level of theory, with the projector augmented wave method together with the BEEF-vdW functional [23,24] as implemented in the GPAW software. [36,37] A k-point sampling relevant for the specific structure, a grid-spacing of 0.18 Å, a vacuum of 10 Å was applied, and all the structures were relaxed to a force below 0.05 eV/Å.

Structures with total energies, ensembles, and the plotting method are available on the webpage (`http://nano.ku.dk/english/research/theoretical-electrocatalysis/katladb/`), including the script to run the microkinetic model.

Keywords

CO_2 reduction,
CO reduction,
Fischer–Tropsh,
Electrochemistry,
Aprotic

References

(1) Chu, S.; Cui, Y.; Liu, N. The path towards sustainable energy. *Nature Materials* **2017**, *16*, 16–22.

(2) Gokhale, A. A.; Dumesic, J. A.; Mavrikakis, M. On the Mechanism of Low-Temperature Water Gas Shift Reaction on Copper. *Journal of the American Chemical Society* **2008**, *130*, 1402–1414.

(3) Fischer, F.; Tropsch, H. The synthesis of petroleum at atmospheric pressures from gasification products of coal. *Brennstoff-Chemie* **1926**, *7*, 97–104.

(4) Schulz, H. Short history and present trends of Fischer–Tropsch synthesis. *Applied Catalysis A: General* **1999**, *186*, 3–12.

(5) Studt, F.; Sharafutdinov, I.; Abild-Pedersen, F.; Elkjær, C. F.; Hummelshøj, J. S.; Dahl, S.; Chorkendorff, I.; Nørskov, J. K. Discovery of a Ni-Ga catalyst for carbon dioxide reduction to methanol. *Nature Chemistry* **2014**, *6*, 320–324.

(6) Behrens, M.; Studt, F.; Kasatkin, I.; Kühl, S.; Hävecker, M.; Abild-Pedersen, F.; Zander, S.; Girgsdies, F.; Kurr, P.; Kniep, B.-L.; Tovar, M.; Fischer, R. W.; Nørskov, J. K.; Schlögl, R. The Active Site of Methanol Synthesis over Cu/ZnO/Al2O3 Industrial Catalysts. *Science* **2012**, *336*, 893–897.

(7) Luk, H. T.; Mondelli, C.; Ferré, D. C.; Stewart, J. A.; Pérez-Ramírez, J. Status and prospects in higher alcohols synthesis from syngas. *Chem. Soc. Rev.* **2017**, *46*, 1358–1426.

(8) Seh, Z. W.; Kibsgaard, J.; Dickens, C. F.; Chorkendorff, I.; Nørskov, J. K.; Jaramillo, T. F. Combining theory and experiment in electrocatalysis: Insights into materials design. *Science* **2017**, *355*.

(9) Ledezma-Yanez, I.; Díaz-Morales, O.; Figueiredo, M. C.; Koper, M. T. M. Hydrogen Oxidation and Hydrogen Evolution on a Platinum Electrode in Acetonitrile. *ChemElectroChem* **2015**, *2*, 1612–1622.

(10) Bagger, A.; Arnarson, L.; Hansen, M. H.; Spohr, E.; Rossmeisl, J. Electrochemical CO Reduction: A Property of the Electrochemical Interface. *Journal of the American Chemical Society* **2019**, *141*, 1506–1514.

(11) Suárez-Herrera, M. F.; Costa-Figueiredo, M.; Feliu, J. M. Voltammetry of Basal Plane Platinum Electrodes in Acetonitrile Electrolytes: Effect of the Presence of Water. *Langmuir* **2012**, *28*, 5286–5294.

(12) Ikeda, S.; Takagi, T.; Ito, K. Selective Formation of Formic Acid, Oxalic Acid, and Carbon Monoxide by Electrochemical Reduction of Carbon Dioxide. *Bulletin of the Chemical Society of Japan* **1987**, *60*, 2517–2522.

(13) Rohr, B. A.; Singh, A. R.; Gauthier, J. A.; Statt, M. J.; Nørskov, J. K. Micro-kinetic model of electrochemical carbon dioxide reduction over platinum in non-aqueous solvents. *Phys. Chem. Chem. Phys.* **2020**, *22*, 9040–9045.

(14) Costentin, C.; Robert, M.; Savéant, J.-M. Catalysis of the electrochemical reduction of carbon dioxide. *Chem. Soc. Rev.* **2013**, *42*, 2423–2436.

(15) Figueiredo, M. C.; Ledezma-Yanez, I.; Koper, M. T. M. In Situ Spectroscopic Study of CO2 Electroreduction at Copper Electrodes in Acetonitrile. *ACS Catalysis* **2016**, *6*, 2382–2392.

(16) Piontek, S.; junge Puring, K.; Siegmund, D.; Smialkowski, M.; Sinev, I.; Tetzlaff, D.; Roldan Cuenya, B.; Apfel, U.-P. Bio-inspired design: bulk iron–nickel sulfide allows for efficient

solvent-dependent CO2 reduction. *Chem. Sci.* **2019**, *10*, 1075–1081.

(17) Ohta, K.; Kawamoto, M.; Mizuno, T.; Lowy, D. A. Electrochemical reduction of carbon dioxide in methanol at ambient temperature and pressure. *Journal of Applied Electrochemistry* **1998**, *28*, 717–724.

(18) Tomita, Y.; Teruya, S.; Koga, O.; Hori, Y. Electrochemical reduction of carbon dioxide at a platinum electrode in acetonitrile-water mixtures. *Journal of the Electrochemical Society* **2000**, *147*, 4164–4167.

(19) Bagger, A.; Ju, W.; Varela, A. S.; Strasser, P.; Rossmeisl, J. Electrochemical CO2 Reduction: A Classification Problem. *ChemPhysChem* **2017**, *18*, 3266–3273.

(20) Hori, Y. In *Modern Aspects of Electrochemistry*; Vayenas, C. G., White, R. E., Gamboa-Aldeco, M. E., Eds.; Springer New York: New York, NY, 2008; pp 89–189.

(21) Hori, Y.; Wakebe, H.; Tsukamoto, T.; Koga, O. Electrocatalytic process of CO selectivity in electrochemical reduction of CO2 at metal electrodes in aqueous media. *Electrochimica Acta* **1994**, *39*, 1833 – 1839.

(22) Gennaro, A.; Isse, A. A.; Severin, M.-G.; Vianello, E.; Bhugun, I.; Savéant, J.-M. Mechanism of the electrochemical reduction of carbon dioxide at inert electrodes in media of low proton availability. *J. Chem. Soc., Faraday Trans.* **1996**, *92*, 3963–3968.

(23) Wellendorff, J.; Lundgaard, K. T.; Møgelhøj, A.; Petzold, V.; Landis, D. D.; Nørskov, J. K.; Bligaard, T.; Jacobsen, K. W. Density functionals for surface science: Exchange-correlation model development with Bayesian error estimation. *Phys. Rev. B* **2012**, *85*, 235149.

(24) Medford, A. J.; Wellendorff, J.; Vojvodic, A.; Studt, F.; Abild-Pedersen, F.; Jacobsen, K. W.; Bligaard, T.; Nørskov, J. K. Assessing the reliability of calculated catalytic ammonia synthesis rates. *Science* **2014**, *345*, 197–200.

(25) Schumacher, N.; Andersson, K.; Grabow, L.; Mavrikakis, M.; Nerlov, J.; Chorkendorff, I. Interaction of carbon dioxide with Cu overlayers on Pt(111). *Surface Science* **2008**, *602*, 702–711.

(26) Schwarz, H. A.; Dodson, R. W. Reduction potentials of CO2- and the alcohol radicals. *The Journal of Physical Chemistry* **1989**, *93*, 409–414.

(27) Kuhl, K. P.; Cave, E. R.; Abram, D. N.; Jaramillo, T. F. New insights into the electrochemical reduction of carbon dioxide on metallic copper surfaces. *Energy Environ. Sci.* **2012**, *5*, 7050–7059.

(28) Peterson, A. A.; Abild-Pedersen, F.; Studt, F.; Rossmeisl, J.; Nørskov, J. K. How copper catalyzes the electroreduction of carbon dioxide into hydrocarbon fuels. *Energy Environ. Sci.* **2010**, *3*, 1311–1315.

(29) Katayama, Y.; Nattino, F.; Giordano, L.; Hwang, J.; Rao, R. R.; Andreussi, O.; Marzari, N.; Shao-Horn, Y. An In Situ Surface-Enhanced Infrared Absorption Spectroscopy Study of Electrochemical CO2 Reduction: Selectivity Dependence on Surface C-Bound and O-Bound Reaction Intermediates. *The Journal of Physical Chemistry C* **2019**, *123*, 5951–5963.

(30) Bagger, A.; Arán-Ais, R. M.; Halldin Stenlid, J.; Campos dos Santos, E.; Arnarson, L.; Degn Jensen, K.; Escudero-Escribano, M.; Roldan Cuenya, B.; Rossmeisl, J. Ab Initio Cyclic Voltammetry on Cu(111), Cu(100) and Cu(110) in Acidic, Neutral and Alkaline Solutions. *ChemPhysChem* **2019**, *20*, 3096–3105.

(31) Nakagawa, S.; Kudo, A.; Azuma, M.; Sakata, T. Effect of pressure on the electrochemical reduction of CO2 on Group VIII metal electrodes. *Journal of Electroanalytical Chemistry and Interfacial Electrochemistry* **1991**, *308*, 339–343.

(32) Hara, K.; Kudo, A.; Sakata, T. Electrochemical reduction of carbon dioxide under high pressure on various electrodes in an aqueous electrolyte. *Journal of Electroanalytical Chemistry* **1995**, *391*, 141–147.

(33) Hara, K.; Tsuneto, A.; Kudo, A.; Sakata, T. Electrochemical Reduction of CO2 on a Cu Electrode under High Pressure: Factors that Determine the Product Selectivity. *Journal of the Electrochemical Society* **1994**, *141*, 2097–2103.

(34) Melchaeva, O.; Voyame, P.; Bassetto, V. C.; Prokein, M.; Renner, M.; Weidner, E.; Petermann, M.; Battistel, A. Electrochemical Reduction of Protic Supercritical CO2 on Copper Electrodes. *ChemSusChem* **2017**, *10*, 3660–3670.

(35) Larsen, A. H. et al. The atomic simulation environment—a Python library for working with atoms. *Journal of Physics: Condensed Matter* **2017**, *29*, 273002.

(36) Mortensen, J. J.; Hansen, L. B.; Jacobsen, K. W. Real-space grid implementation of the projector augmented wave method. *Phys. Rev. B* **2005**, *71*, 035109.

(37) Enkovaara, J. et al. Electronic structure calculations with GPAW: a real-space implementation of the projector augmented-wave method. *Journal of Physics: Condensed Matter* **2010**, *22*, 253202.

(38) Ayawei, N.; Ebelegi, A. N.; Wankasi, D. Modelling and Interpretation of Adsorption Isotherms. *Journal of Chemistry* **2017**, 1–11.

(39) Bligaard, T.; Nørskov, J.; Dahl, S.; Matthiesen, J.; Christensen, C.; Sehested, J. The Brønsted–Evans–Polanyi relation and the volcano curve in heterogeneous catalysis. *Journal of Catalysis* *224*, 206–217.

(40) Exner, K. S. Paradigm change in hydrogen electrocatalysis: The volcano's apex is located at weak bonding of the reaction intermediate. *International Journal of Hydrogen Energy* *45*, 27221–27229.

(41) Marshall, A. T. Using microkinetic models to understand electrocatalytic reactions. *Current Opinion in Electrochemistry* *7*, 75–80.

Catalytic CO_2/CO Reduction: Gas, Aqueous and Aprotic phase.

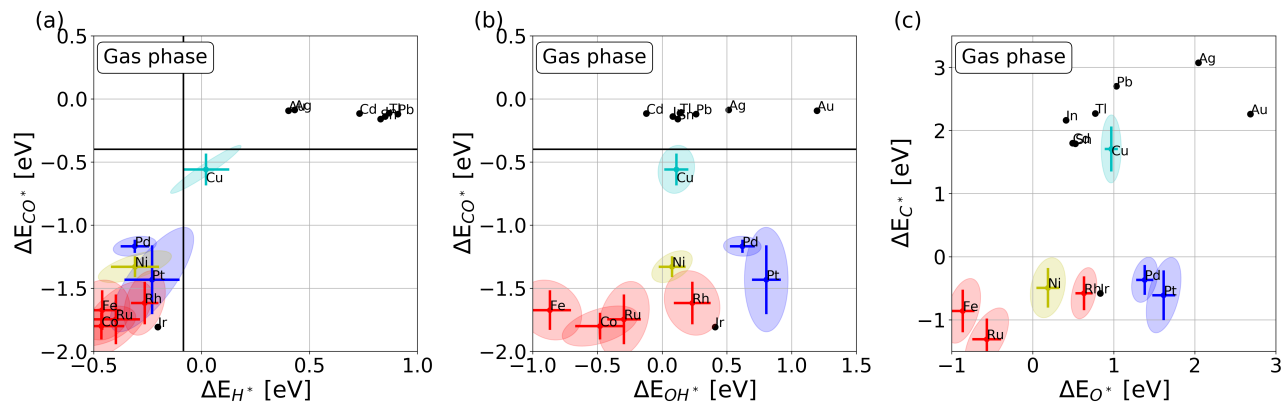Alexander Bagger, Oliver Christensen, Vladislav Ivaništšev and Jan Rossmeisl

Figure S1: (a) CO vs. H, (b) CO vs. OH, and (c) C vs. O descriptor analysis for the gas-phase products given in the periodic table in Figure 1a.
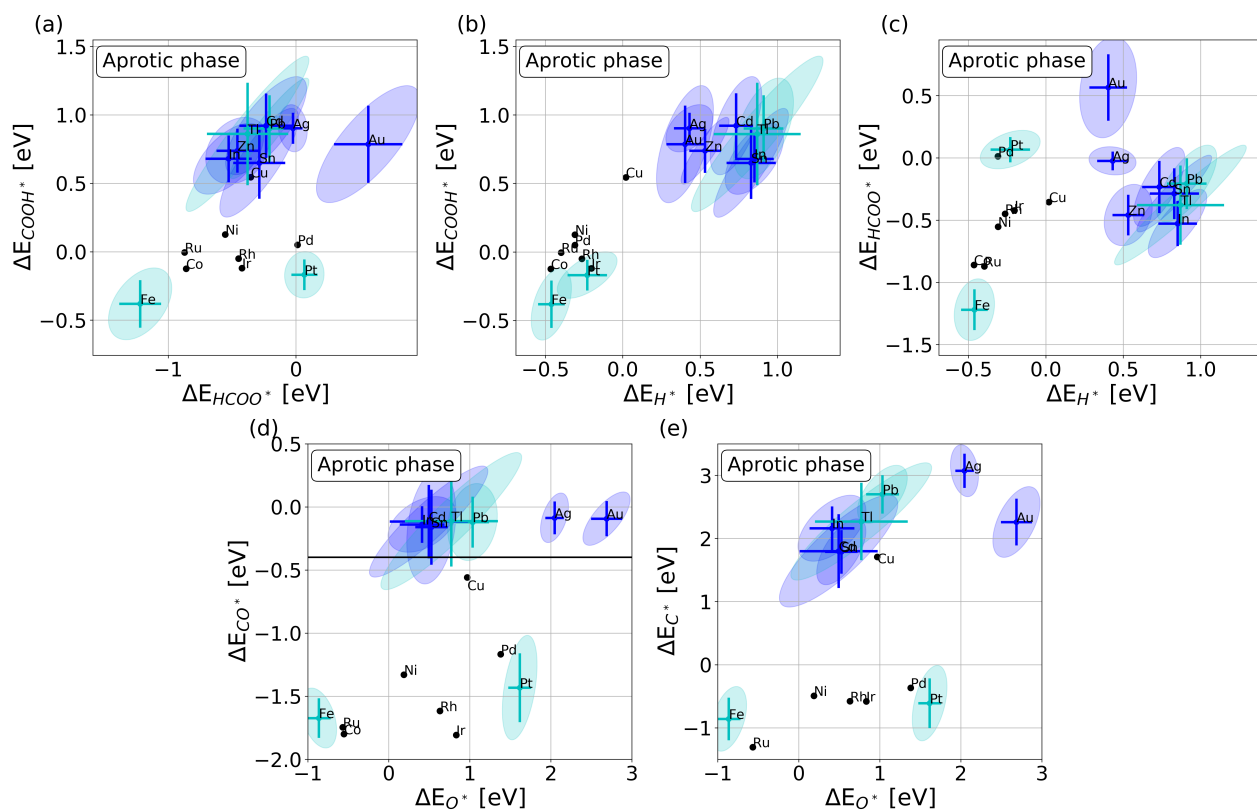

Figure S2: (a) COOH vs. HCOO, (b) COOH vs. H, (c) HCOO vs. H, (d) CO vs. O, and (e) C vs. O descriptor analysis for the aprotic phase products given in the periodic table in Figure 1c.
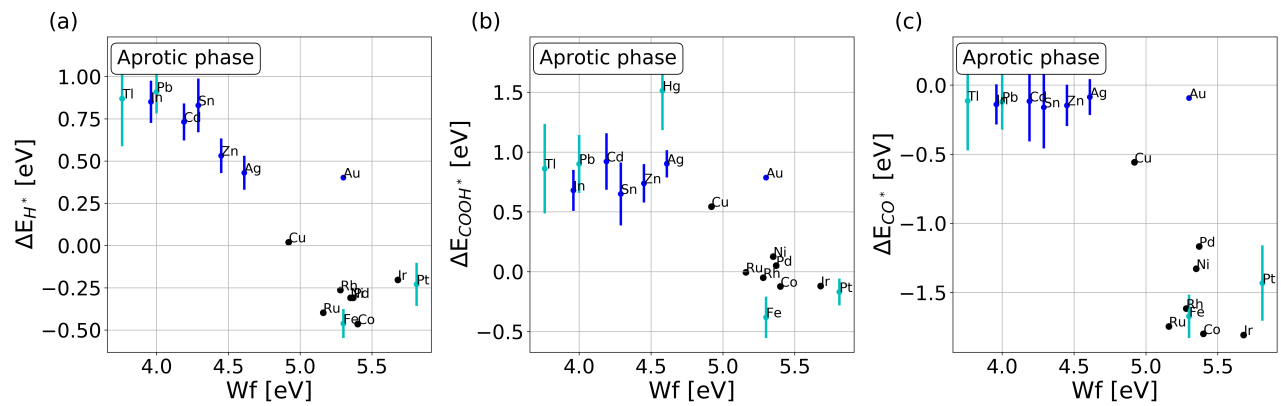
Figure S3: (a) H vs. work function, (b) COOH vs. work function, and (c) CO vs. work function descriptor analysis for the aprotic phase products given in the periodic table in Figure 1c.

Microkinetic model

Our microkinetic model employs four rate expressions 11–14 for the H_2, CO, HCOOH, and C_2O_4 formation:

$$r_{H_2} = \theta \cdot k_{H_2} \cdot n_{H_2O}^2 \cdot \exp\left(-\frac{\Delta E_{H^*}}{k_B T}\right) \tag{11}$$

$$r_{CO} = \theta \cdot k_{CO} \cdot n_{CO_2}^2 \cdot \exp\left(-\frac{\Delta E_{CO_2^*}}{k_B T} + \frac{\Delta E_{CO^*}}{k_B T}\right) \tag{12}$$

$$r_{HCOOH} = \theta \cdot k_{HCOOH} \cdot n_{H_2O} \cdot n_{CO_2} \cdot \exp\left(-\frac{\Delta E_{CO_2^*}}{k_B T}\right) \tag{13}$$

$$r_{C_2O_4} = \theta^2 \cdot k_{C_2O_4} \cdot n_{CO_2}^2 \cdot \exp\left(-\frac{2\Delta E_{CO_2^*}}{k_B T}\right) \tag{14}$$

where k_{H_2}, k_{CO}, k_{HCOOH} and $k_{C_2O_4}$ are four parameters to adjust the absolute rates, n_{H_2O} and n_{CO_2} are the concentration or pressure, ΔE_{H^*}, $\Delta E_{CO_2^*}$ and ΔE_{CO^*} are the respective binding energies, θ is the number of free sites, and $k_B T$ is the product of the Boltzmann constant and temperature.

When deriving Eqs.11–14:

1. We assume H_2O to be in equilibrium with $(H^+ + e^-)$;

2. We only consider high overpotential (low absolute potential);

3. We only account for forward reaction rates;

4. We use Henry isotherm to describe the adsorption;[38]

5. We apply Bell–Evans–Polanyi (BEP) relation with the coefficient of 1 for estimating the reaction barriers;[39]

6. We approximate barriers for the desorption process and all free energies with corresponding dinging energy values (ΔE).

The first assumption allows us to use the water concentration as a probe for the proton reactions. The second assumption allows us to assume that the electron transfer to CO_2 is always possible, and the reaction is only limited by the CO_2 and H_2O concentrations in the solution. *Et seq.* assumptions simplify the derivation of Eqs. 11–14.

Hydrogen evolution reaction

For hydrogen evolution, the proton concentration is proportional to the water content in solution and its reduction reaction is rather well known:

$$2\,(H^+ + e^-) + * \longrightarrow (H^+ + e^-) + H^* \longrightarrow H_2 \tag{16}$$
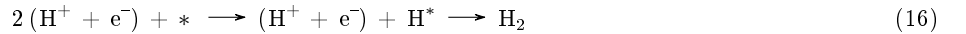
Here we equalize the activation energy barrier to the H^+ binding energy using the BEP relation and assuming weak bonding of the reaction intermediate.[40] An overview of different microkinetic modeling approaches can be found in Ref. 41.
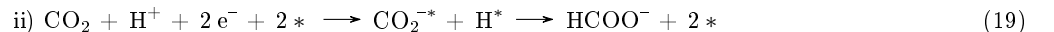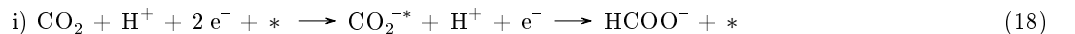
Oxalic acid formation

For oxalic acid, the reaction is straightforward, as it is only two CO_2 molecules reacting with each other:

$$2\,CO_2 + 2\,e^- + 2* \longrightarrow 2\,CO_2^{-*} \longrightarrow C_2O_4^{2-} \tag{17}$$
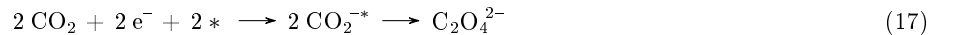
Here we equalize the activation energy to the double of CO_2^{-*} binging energy assuming that the C—C bond formation is barrierless and $\Delta E_{C_2O_4^*} \approx 2\Delta E_{CO_2^*}$.

Formic acid formation

For formic acid (HCOOH), we consider the reaction toward $HCOO^-$ as this is probably the produced species in experiments (with $pH > pK_a(HCOOH)$). Among various possible pathways, we tested the following two:

$$\text{i) } CO_2 + H^+ + 2\,e^- + * \longrightarrow CO_2^{-*} + H^+ + e^- \longrightarrow HCOO^- + * \tag{18}$$

$$\text{ii) } CO_2 + H^+ + 2\,e^- + 2* \longrightarrow CO_2^{-*} + H^* \longrightarrow HCOO^- + 2* \tag{19}$$

To derive Eq. 13, we use the pathway 18 , as it shows acceptable agreement with the experimental data.
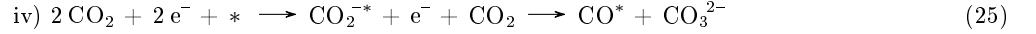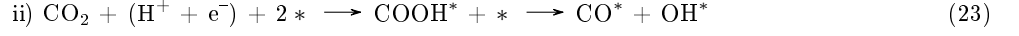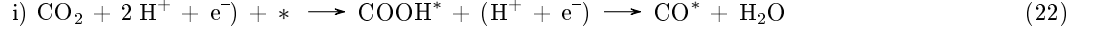
Carbon monoxide formation

For the formation of CO, there are also several reaction paths, and CO also needs to be able to dissociate from the surface. Getting CO to dissociate from the surface is determined by:

$$CO^* \longrightarrow CO_{(g)} + * \tag{20}$$

$$r_{CO} = \theta_{CO^*} \cdot k'_{CO} \cdot \exp\left(\frac{\Delta E_{CO}}{k_B T}\right) \tag{21}$$

The most crucial part of our model is the pathway choice for the forward reaction from CO_2 to CO^*. Among various possible pathways, we tested the following four:

$$\text{i) } CO_2 + 2\,H^+ + e^-) + * \longrightarrow COOH^* + (H^+ + e^-) \longrightarrow CO^* + H_2O \tag{22}$$

$$\text{ii) } CO_2 + (H^+ + e^-) + 2* \longrightarrow COOH^* + * \longrightarrow CO^* + OH^* \tag{23}$$

$$\text{iii) } CO_2 + 2* \longrightarrow CO^* + O^* \tag{24}$$

$$\text{iv) } 2\,CO_2 + 2\,e^- + * \longrightarrow CO_2^{-*} + e^- + CO_2 \longrightarrow CO^* + CO_3^{2-} \tag{25}$$

The pathway 25 showed the greatest agreement with the experimental data and is thus used in our model. Herewith, the reactions toward OH* (23) and O* (24) can cause the competing reduction to water.

In total, we consider the adsorption species of H, CO, and CO_2 at the surface. We do not consider reaction pathways 23 and 24 that produce OH* and O* at the surface, and we do also not consider CO_3^{2-}, HCO_3^-, or $HCOO^-$ to adsorb at the surface at these low potentials. Hence, the number of free sites on the surface is then given by:

$$\theta = 1 - \theta_{H^*} - \theta_{CO^*} - \theta_{CO_2^*} = \frac{1}{1 + n_{H_2O} \cdot \exp\left(-\frac{\Delta E_{H^*}}{k_B T}\right) + n_{CO} \cdot \exp\left(-\frac{\Delta E_{CO^*}}{k_B T}\right) + n_{CO_2} \cdot \exp\left(-\frac{\Delta E_{CO_2^*}}{k_B T}\right)} \tag{26}$$

Combination of pathways 16–18, and 25 gives rate expressions 11–14, which in turn are visualized in Figures 2–4 (for discussion, see the article).